Microstructure and Texture Evolution of Hot-Rolled Mg-3Gd Alloy during Recrystallization

Fang Han [1], Hanxi Wang [1], Xuan Luo [1,2], Ziyong Hou [1,*], Guilin Wu [3] and Xiaoxu Huang [1,4,*]

1 International Joint Laboratory for Light Alloys (MOE), College of Materials Science and Engineering, Chongqing University, Chongqing 400044, China; fanghan@cqu.edu.cn (F.H.); shuangshangwhx@163.com (H.W.); luo.xuan@njtech.edu.cn (X.L.)
2 Key Laboratory for Light-Weight Materials, Nanjing Tech University, Nanjing 210009, China
3 Beijing Advanced Innovation Center for Materials Genome Engineering, University of Science and Technology Beijing, Beijing 100083, China; guilinwu@ustb.edu.cn
4 Shenyang National Laboratory for Materials Science, Chongqing University, Chongqing 400044, China
* Correspondence: houzy@cqu.edu.cn (Z.H.); xiaoxuhuang@cqu.edu.cn (X.H.)

Abstract: An Mg-3Gd (wt.%) sample with gradient rolling strains (ε = 0–0.55) was prepared using a wedge-shaped plate after one-pass hot rolling, allowing a high-throughput characterization of microstructure and texture over a wide strain range within one hot-rolled plate. The microstructure and texture evolutions were characterized as a function of rolling strain for the as-hot-rolled sample and as a function of annealing temperature for the subsequently annealed samples. The deformed microstructure showed a gradual change with increasing rolling strain, i.e., from a deformation twins-dominant structure in the low strain range of 0–0.20, to a shear bands-dominant structure in the higher strain range of 0.20–0.55. The recrystallization behavior during annealing showed a clear correlation between the recrystallization nucleation site and the deformed microstructure. However, a weak recrystallization texture with non-basal texture components was formed over almost the entire strain range. This work demonstrates a high-throughput experimental strategy using a wedge-shaped sample to investigate the effect of various processing parameters, such as strain and annealing temperature, on the evolution of microstructure, texture, and mechanical properties, which could accelerate the optimization of processing parameters and microstructural design.

Keywords: Mg-3Gd; high-throughput characterization; deformed microstructure; recrystallization behavior; processing parameter

1. Introduction

Rolling is one of the most crucial fabrication and processing techniques for magnesium (Mg) alloys [1,2]. In hexagonal close-packed (HCP) Mg alloys, basal $\{0001\} < 11\bar{2}0 >$ slip with the lowest critical shear stress (CRSS) always results in the formation of strong basal textures and mechanical anisotropy after rolling, which limits the applications of Mg alloys [3,4]. To solve this issue and promote the homogenization of microstructure in Mg alloys, a large amount of work has been performed. Interestingly, the addition of rare-earth (RE) elements, e.g., Y, Gd, Ce, La and Nd, in Mg alloys can highly decrease the intensity of basal textures, anisotropy, and asymmetry, owing to the formation of a weak texture component during recrystallization [5–7]. It is well known that shear bands [8], twin boundaries [9], and particles [10] are the preferential recrystallization nucleation sites for enhancing the formation of a weak recrystallization texture in Mg-RE alloys [11,12]. Meanwhile, the recrystallization behavior of Mg alloys is also highly dependent on the degree of strain [13,14]. In particular, the activation of tension twins (TTWs) and basal ships is much easier than that of compression twins (CTWs), double twins (DTWs), and non-basal slips during the early stage of plastic deformation [15–17]. With increasing strain, the volume fraction of CTWs and DTWs increases while that of TTWs decreases. Moreover, under large

strains, non-basal slips are enhanced [18], followed by the formation of high-density shear bands [19,20]. Therefore, the deformed microstructures have a substantial effect on the subsequent recrystallization nucleation and grain growth in Mg alloys [21–23]. However, a complete characterization of the recrystallization process by tracking microstructural evolution at specific plastic strains and annealing conditions is extremely tedious since a large amount of experimental data is required from the same experiment. The effects of rolling strain on the deformation microstructure and recrystallization behavior were mainly assessed using homogeneous materials [21,24–26]. To some extent, such experiments were time-consuming and costly. Wedge-plate rolling provides an efficient alternative strategy, which has been used to study the effect of initial texture on recrystallization and twinning-induced recrystallization behavior of AZ31 Mg alloy during hot rolling [22,27]. This high-throughput approach also provides a possibility for studying the formation of weak texture in Mg-RE alloys using one wedge-plate sample. However, the high-throughput approach has rarely been employed to understand the microstructure and recrystallization of Mg-RE alloys [28,29].

In this work, we applied a wedge-plate rolling approach to obtain a sample with a large strain gradient. The microstructural evolution and recrystallization behavior during hot rolling and annealing were thoroughly investigated using the sample. The results showed that wedge-plate rolling can feasibly be used to study the effect of deformation strains on the recrystallization behavior, and to help to screen the range of optimized processing parameters in an efficient way.

2. Materials and Experimental Procedures

2.1. Materials

An Mg-3Gd (wt.%) slab-like billet was prepared by a high-frequency induction melting of pure Mg and Mg-7.5Gd (wt.%) alloy in an atmosphere of SF_6/CO_2 (1:99). The sample with a dimension of $65 \times 34 \times 10$ mm^3 was cut from the billet and homogenized at 450 °C for 24 h, then quenched in water. The homogenized sample consisted of coarse grains, of approximately millimeter (mm) scale, as shown in Figure 1a. The {0002} pole figure shows all grains had rather scattered orientations, noting that the high intensity of specific poles was caused by the presence of only a few coarse grains (Figure 1a,b). The homogenized sample was further cut into a wedged plate, with a thickness variation of 3–10 mm from one end to the other (Figure 2). The engineering strain was calculated based on the volume invariant principle and evaluated by $\varepsilon = (t_0 - t)/t_0$, where t_0 and t were the thicknesses before and after rolling. The wedged plate was preheated at 400 °C for 10 min and then rolled to $\sim$3 mm, corresponding to a maximum engineering strain, $\varepsilon_{max} = 0.7$, by one pass using a conventional two-roller miller. Finally, a sample with a strain variation from 0 to 0.7 was obtained. However, only the section of the sample with engineering strains in the range of $\varepsilon = 0$–0.55 was used in the present study since a crack occurred at the high-strain end. The rolled sample was then annealed for 1 h at temperatures ranging from 200 to 375 °C for a temperature interval of 25 °C. All the rolled and annealed samples were quenched in water.

2.2. Microhardness Test and Microstructure Analysis

The microhardness was measured using a Vickers microhardness tester (HMV-G21ST, SHIMADZU, Kyoto, Japan) with a load of 50 g and a dwell time of 10 s. An average value from 10 tests of each rolling strain was used. The microstructure of the whole rolled sample was observed using a light optical microscope (LOM, Zeiss Axio Vert.A1, ZEISS, Oberkochen, Germany). The samples for LOM observations were ground, electro-polished, and etched via an acetal-picric mixture (10 mL acetic acid, 4.2 g picric acid, 20 mL H_2O, 70 mL ethanol) for 10–15 s. Furthermore, the microstructures of rolled and annealed samples with specific rolling strain were examined using an Oxford electron backscatter diffraction (EBSD) detector installed on a scanning electron microscope (SEM, JEOL JSM-7800F, Tokyo, Japan), operated at 20 kV. EBSD samples were prepared by mechanical

grinding and electro-polished using a perchloric acid and ethanol solution (1:9) at 20 V and −30 °C for 60 s. The LOM, EBSD investigations, and microhardness test were conducted on the rolling direction (RD)–normal direction (ND) plane. The regions of interest (ROI) for EBSD and microhardness were focused on the different strains from 0.05 to 0.55 with a strain interval of 0.05. To quantify the twins volume fraction and average grain size ($\bar{d}$), the HKL Channel 5 software was used for the EBSD data. The recrystallized grains in the annealed samples were extracted from EBSD data of 1000×1500 μm^2 based on the grain orientation spread (GOS) criterion of less than 2° [30,31]. Global textures were examined on the rolling plane (containing the RD and the transverse direction, TD) of the samples using an X-ray diffractometer (XRD, Rigaku D/max 2500 PC, RIGAKU, Tokyo, Japan) with Cu Kα radiation under a voltage of 40 kV. The post-calculation of incomplete {0002}, {10$\bar{1}$0}, {10$\bar{1}$1}, and {10$\bar{1}$2} pole figures was conducted using LaboTex 3.0 software (LaboTex, Krakow, Poland).
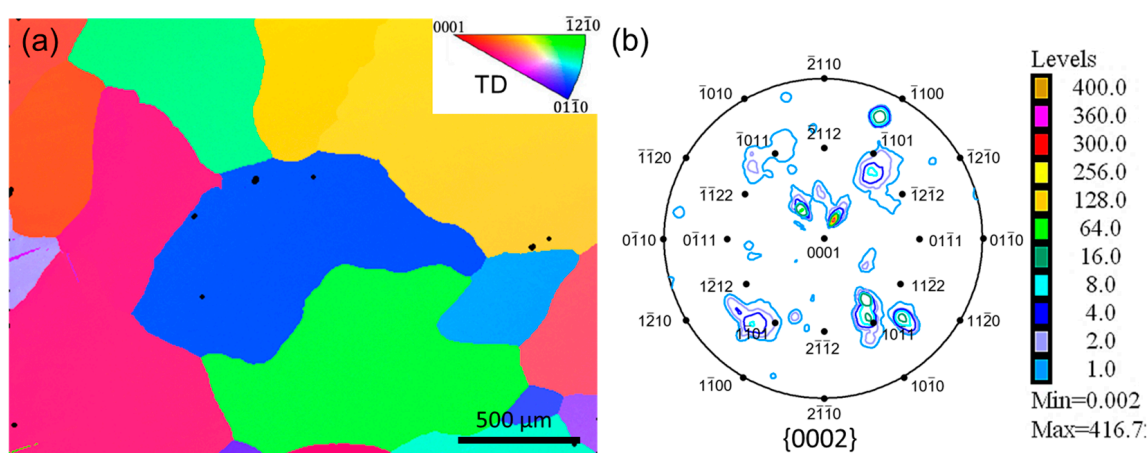

Figure 1. (**a**) EBSD inverse pole figure (IPF) map and (**b**) {0002} pole figure of the homogenized sample. Observation along TD was applied to the IPF triangle.
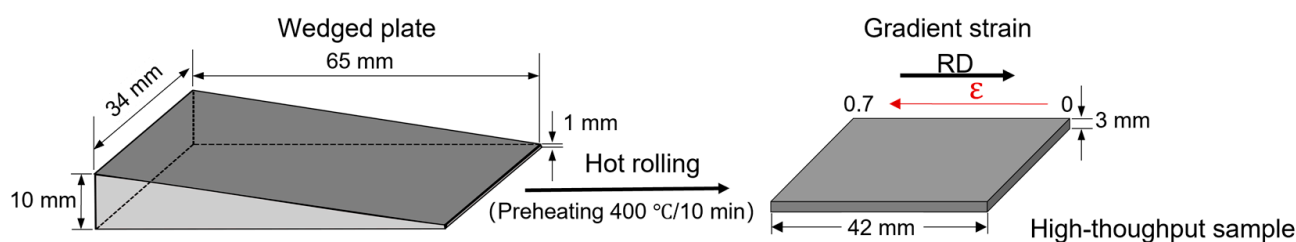

Figure 2. Schematic showing the preparation of a sample with a strain gradient by hot rolling of a wedged sample.

3. Results

3.1. Microstructure and Texture of the As-Hot-Rolled Sample

Figure 3 shows the microstructure of the as-hot-rolled sample with ε = 0–0.55. The variation of the deformed microstructures along the RD clear transition is seen from a structure containing deformation twins (marked by red arrows) to a structure containing shear bands (marked by black arrows). In the low-strain regions (ε < 0.20) in Figure 3a, a large number of deformation twins were found inside the original coarse grains. As the rolling strain increases (ε ≥ 0.20), typical shear bands with increasing amount became the main feature instead of the deformation twins. Figure S1 provided in the Supplementary Material shows more detailed variations in the microstructural features with strain. In summary, deformation twins and shear bands are the two apparent microstructural features and their corresponding volume fractions were strongly dependent on the rolling strain.
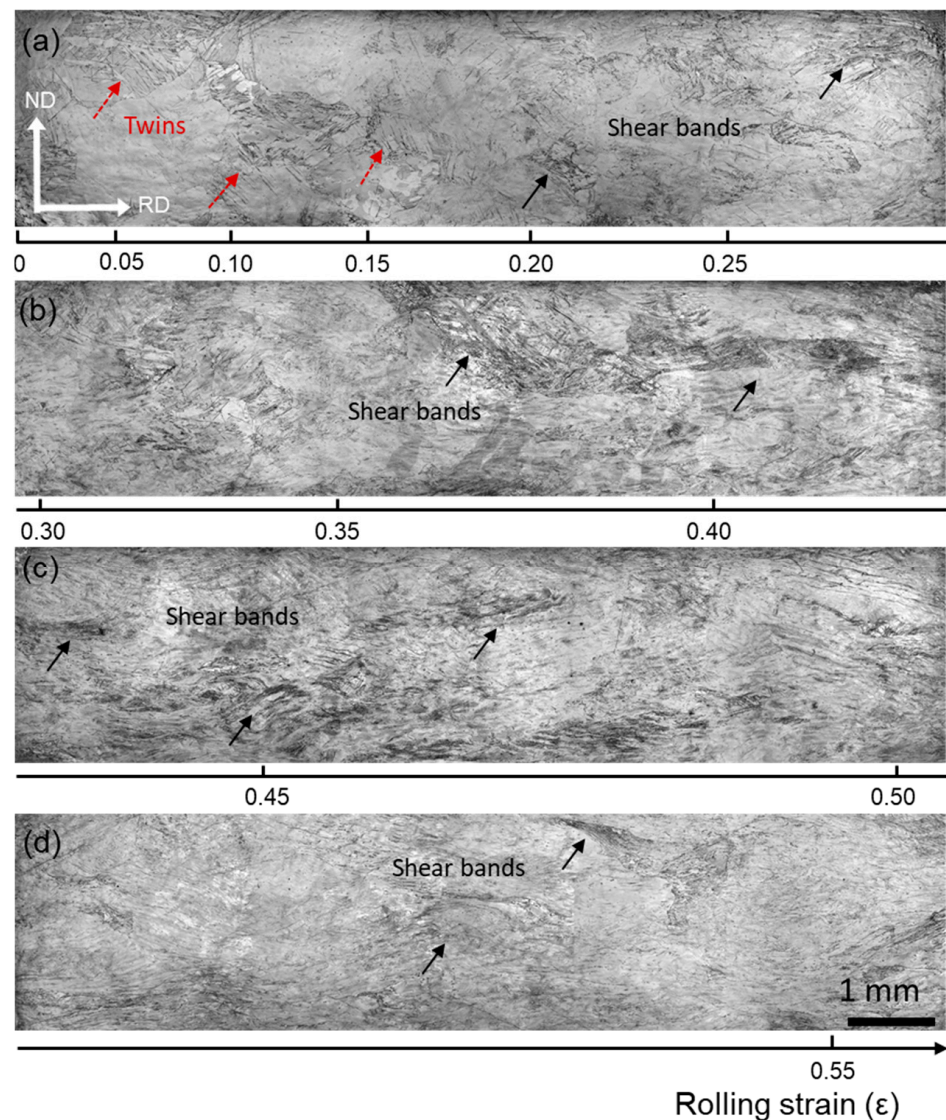
Figure 3. (**a–d**) Microstructure of the as-hot-rolled sample with ε = 0–0.55.

Figure 4 shows EBSD maps of the as-hot-rolled sample at selected locations of different strains. High-angle grain boundaries (HAGBs, ≥15°) and low-angle grain boundaries (LAGBs, 3–15°) are colored by black and grey lines, respectively. The type of deformation twins (DTWs) can also be identified by the twin/matrix misorientation. Three common types of DTWs are $\{10\bar{1}2\}$ 86° ± 5°< $11\bar{2}0$ > TTWs, $\{10\bar{1}1\}$ 56° ± 5°< $11\bar{2}0$ > CTWs, and $\{10\bar{1}2\}$–$\{10\bar{1}1\}$ 38° ± 5°< $11\bar{2}0$ > DTWs, colored by red, green, and fuchsia lines, respectively. The EBSD microstructure (Figure 4) is consistent with the LOM microstructure (Figure 3). At a very low strain ε = 0.05, a heterogeneous microstructure is formed containing a large number of TTWs, and few CTWs and DTWs, as shown in Figure 4a. Most TTWs are parallel to each other, while some TTWs interact with each other. In addition, a few straight shear bands were inclined at an angle of about 50° to the RD, marked by blue arrows (Figure 4a). With increasing rolling strain (ε < 0.20), the number of visible TTWs decreased while the number of DTWs increased. More parallel and straight shear bands form symmetric pairs. It should be noted that the TTW-dominated microstructure with visible grain boundaries remains in these deformed regions, as shown in Figure 4b,c. With increasing the rolling strain to 0.20, a high density of shear bands was observed (Figure 4d). Sufficiently high stresses in the high-strain region led to formation of DTWs and re-oriented twins, enhancing the activity of local basal slips and the refinement of twins to form shear

bands [32]. These newly formed shear bands were inserted into grains and caused a change in their initial orientation [33]. With further increasing the rolling strain, the shear bands become wavy instead of parallel and straight, resulting in a high-stress concentration. The inclination angles of shear bands to RD were approximately $\pm 30°$. Meanwhile, multiple dislocation slips were activated, including basal and non-basal slips [33,34]. The high activity of non-basal slips and intensive interaction among dislocations, deformation twins, and shear bands led to a more homogeneous microstructure. The grain boundaries were hardly identified, as shown in Figure 4e–k. In addition, no dynamic recrystallized grains and precipitation occurred during the hot rolling. Therefore, the microstructure in the hot-rolled sample was divided into two categories: deformation twins-dominated structures at $\varepsilon < 0.20$, and shear bands-dominated structures at $\varepsilon \geq 0.20$. The effect of deformed microstructure on the subsequent recrystallization is discussed later in this article.
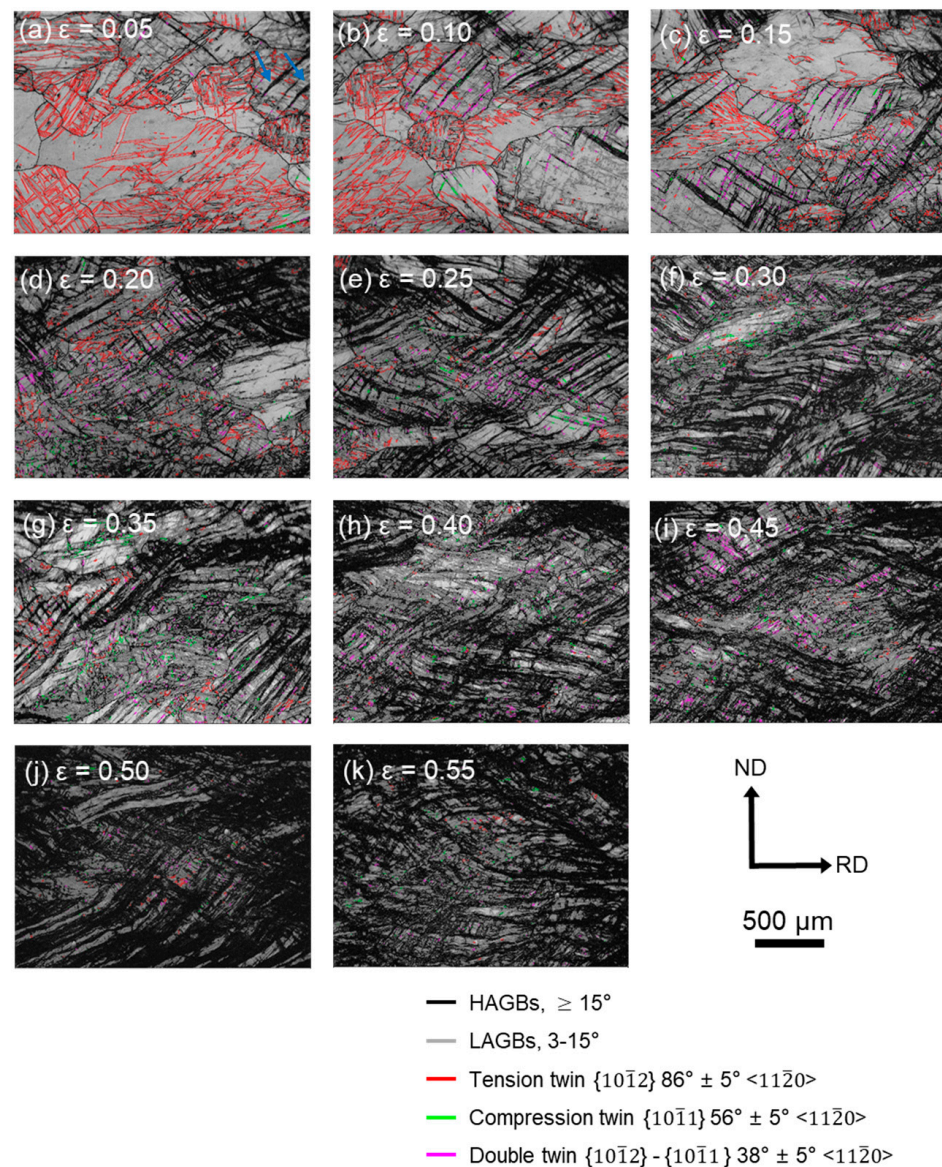

Figure 4. EBSD boundary structure maps of the as-hot-rolled sample at locations of different rolling strains: (**a**) $\varepsilon = 0.05$, (**b**) $\varepsilon = 0.10$, (**c**) $\varepsilon = 0.15$, (**d**) $\varepsilon = 0.20$, (**e**) $\varepsilon = 0.25$, (**f**) $\varepsilon = 0.30$, (**g**) $\varepsilon = 0.35$, (**h**) $\varepsilon = 0.40$, (**i**) $\varepsilon = 0.45$, (**j**) $\varepsilon = 0.50$, (**k**) $\varepsilon = 0.55$. High-angle grain boundaries (HAGBs, $\geq 15°$) and low-angle grain boundaries (LAGBs, 3–15°) are colored by black and grey lines, respectively. $\{10\bar{1}2\}$ $86° \pm 5° < 11\bar{2}0 >$ TTWs, $\{10\bar{1}1\}$ $56° \pm 5° < 11\bar{2}0 >$ CTWs, and $\{10\bar{1}2\}$–$\{10\bar{1}1\}$ $38° \pm 5° < 11\bar{2}0 >$ DTWs are indicated by red, green, and fuchsia lines, respectively.

Figure 5 shows the micro-textures of the as-hot-rolled sample at selected locations of different rolling strains, which were analyzed from the EBSD results. With increasing rolling strain, the spread of texture components towards RD and TD decreased, and basal textures were formed in high-strained regions. Due to the presence of high-density shear bands and dislocations at strains $\varepsilon \geq 0.20$, the indexing rates of EBSD were low. Therefore, the texture analysis of deformed sample is limited. Based on the global textures of high-strain regions determined by XRD, it is easier and more accurate to understand the effect of rolling strains on the deformed textures, as shown in Figure 6. The basal texture component was formed due to the activation of basal slips and TTWs. Moreover, a typical "RD-spilt" texture component was observed in all of the regions. This "RD-spilt" feature has been reported in many rolled or extruded Mg-RE alloys, which is related to the activation of pyramidal <c+a> slips and the occurrence of double twins [19,29,34–36].
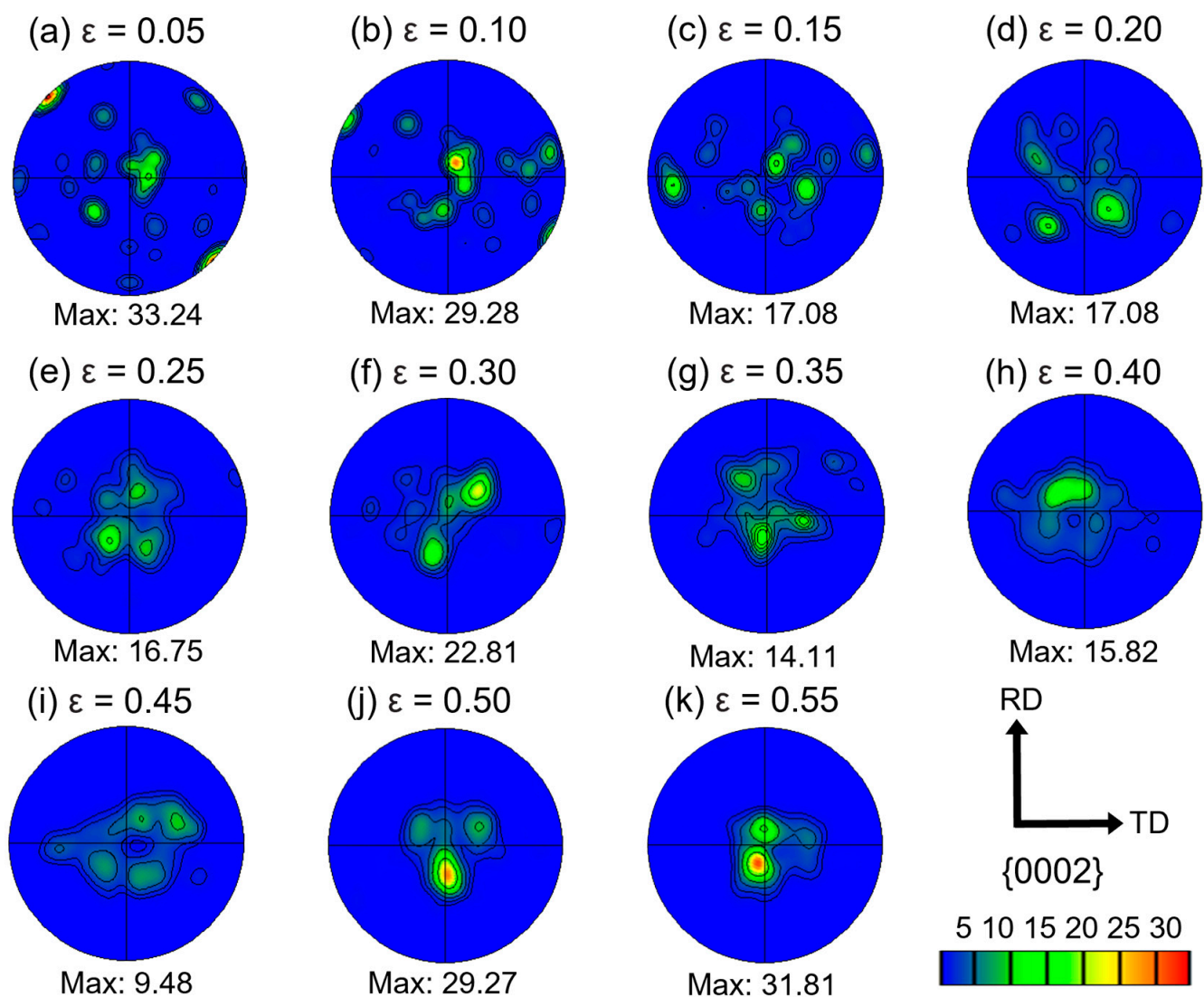

Figure 5. {0002} pole figures of the as-hot-rolled sample with different rolling strains: (**a**) $\varepsilon = 0.05$, (**b**) $\varepsilon = 0.10$, (**c**) $\varepsilon = 0.15$, (**d**) $\varepsilon = 0.20$, (**e**) $\varepsilon = 0.25$, (**f**) $\varepsilon = 0.30$, (**g**) $\varepsilon = 0.35$, (**h**) $\varepsilon = 0.40$, (**i**) $\varepsilon = 0.45$, (**j**) $\varepsilon = 0.50$, (**k**) $\varepsilon = 0.55$.
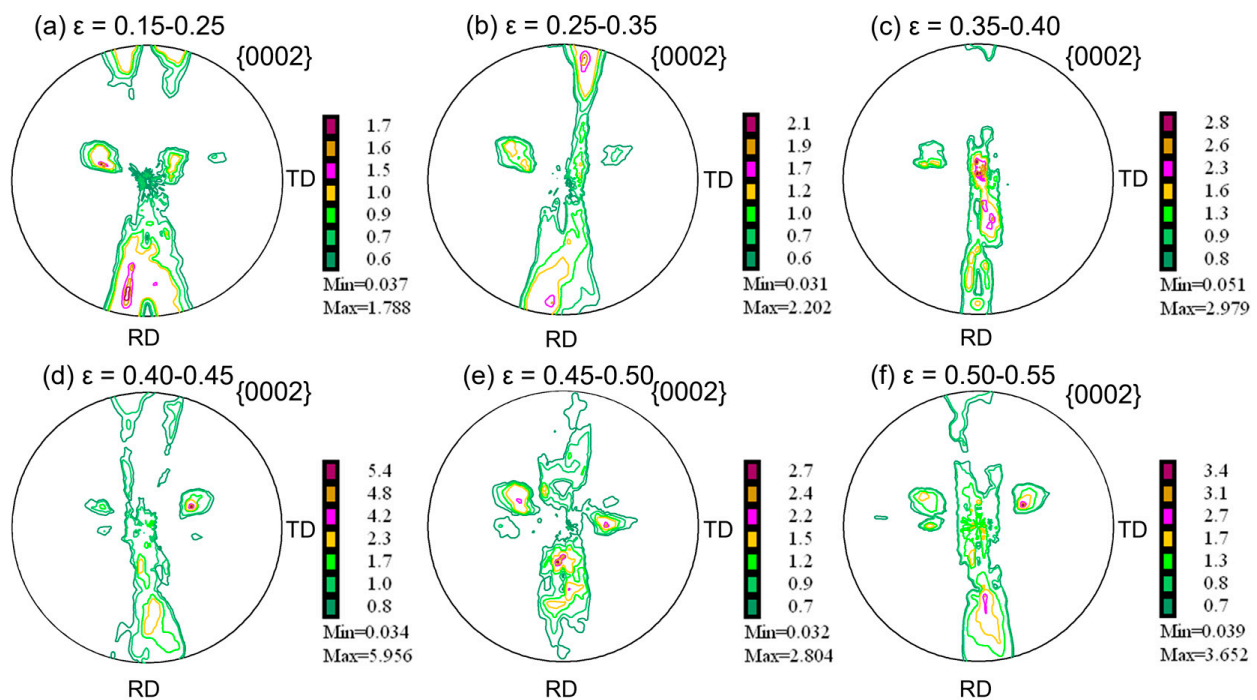
Figure 6. Global texture variation in the as hot-rolled sample with different rolling strains ranging from 0.15 to 0.55: (**a**) ε = 0.15–0.25, (**b**) ε = 0.25–0.35, (**c**) ε = 0.35–0.40, (**d**) ε = 0.40–0.45, (**e**) ε = 0.45–0.50, (**f**) ε = 0.50–0.55.

3.2. Microhardness of Hot-Rolled and Annealed Samples

To evaluate the recrystallization temperature, Vickers microhardness tests were performed at regions with varying strains and after isochronal annealing. Figure 7a shows the microhardness curves of the as-hot-rolled and annealed samples against the rolling strain. With increasing rolling strains from 0 to 0.55, the microhardness of the rolled sample increased from 51 $\pm$ 4 HV to 65 $\pm$ 4 HV. The increment in the microhardness of the rolled sample was mainly caused by the strain hardening response. After annealing for 1 h at 200 °C, a slight annealing hardening response occurred, which was associated with the segregation of Gd elements at different defects, including grain boundaries, twin boundaries, stacking faults, and dislocations [37,38]. During the annealing process, the segregation hardening was in competition with the recovery and recrystallization-induced softening. Annealed at 250 °C, the microhardness of the whole sample was slightly lower than that of the rolled sample. When the annealing temperature increased to 300 °C, an evident softening phenomenon was observed. The decrease in microhardness became more noticeable than that of the annealed sample at 250 °C, especially for the deformed regions with $\varepsilon \geq 0.35$. When the annealing temperature was up to 350 °C, the microhardness of the sample was almost kept constant at different rolling strains. It can be presumed that the recrystallization process occurred in the whole sample. Figure 7b shows the microhardness variation of the rolled sample annealed at different temperatures. The decreasing trend of microhardness at the different rolling strains was similar to the increase in annealing temperature, and the decrease in microhardness at ε = 0.55 was the most among the others. Generally, the temperature where the microhardness decreases to 50% is regarded as the recrystallization temperature [39–41] and the recrystallization behavior of the sample occurs first in the deformed region with the highest rolling strain [42,43]. Therefore, the highest rolling strain (ε = 0.55) should be considered to estimate the lowest recrystallization temperature in the as-hot-rolled sample. Accordingly, 300 °C could be regarded as the recrystallization temperature for the 0.55 rolling strain, marked by an orange arrow in Figure 7b.
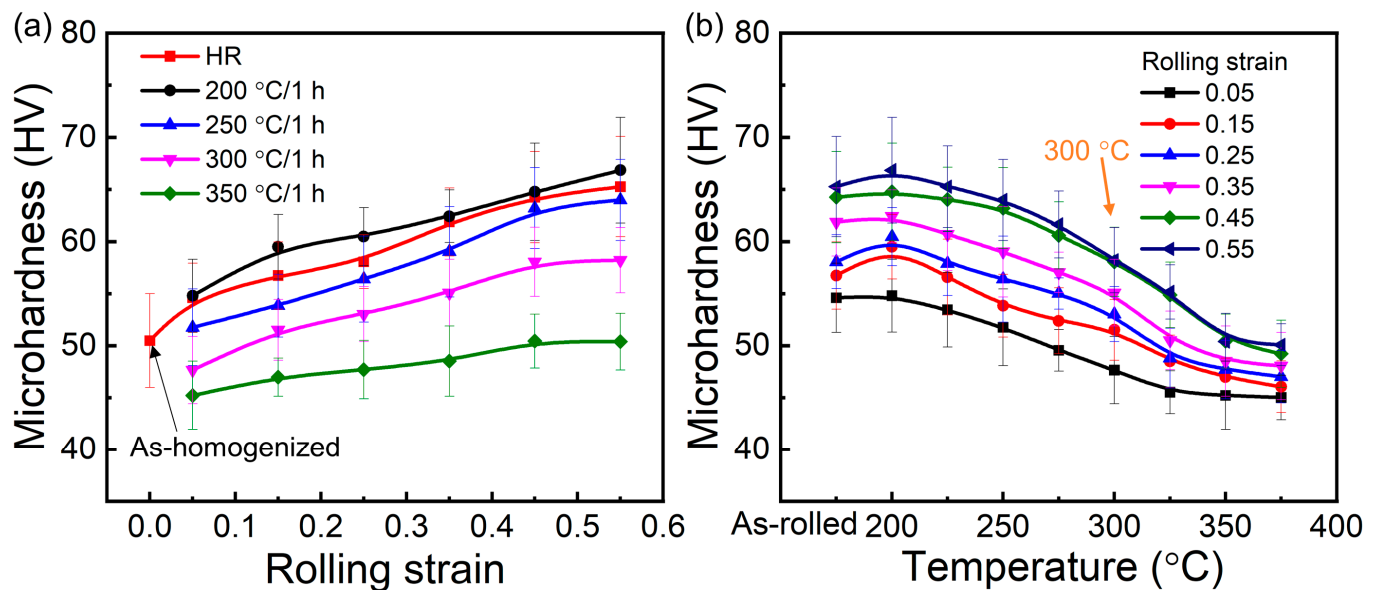
Figure 7. Microhardness curves of hot-rolled and annealed samples: (**a**) the relationship between microhardness and rolling strain at different annealing temperatures, (**b**) the relationship between microhardness and annealing temperature at different rolling strains.

3.3. Microstructure and Texture of the Annealed Sample

　　Considering that the recrystallization temperature determined by the microhardness method is not accurate, the recrystallization microstructure of the rolled sample was observed from a temperature of 275 °C to 350 °C. Figure 8 shows the kernel average misorientation (KAM) maps of the rolled samples with ε = 0.05, 0.15, 0.25, 0.35, 0.45, 0.55 annealed at different temperatures for 1 h. Recrystallized grains, in general, have a small lattice distortion with low KAM values, and the non-indexed black regions could have a higher lattice distortion and local misorientation than the indexed regions in Figure 8. Therefore, the newly nucleated grains were recognized easily by their KAM values. In the region with ε = 0.05, most TTWs remained, and only a few recrystallized grains were formed along CTWs and DTWs during annealing at a temperature range of 275 °C to 350 °C, indicating a static recovery was the dominant behavior during the annealing process. At 275 °C, a few recrystallized grains were formed in the shear bands at rolling strains ε = 0.35, 0.45, 0.55. With the increase in the annealing temperature to 300 °C, a few recrystallized grains were observed in the regions ε = 0.15, 0.25, while the volume fraction of recrystallized grains increased with further increasing the rolling strain. Further increasing the annealing temperature to 325 °C, an evident necklace-like partially recrystallized microstructure was observed along twin boundaries in the region of ε = 0.15. The volume fraction of necklace-like recrystallized grains increased with increasing annealing temperature. For the shear bands-dominated structures with ε = 0.25, 0.35, 0.45, 0.55, the potential nucleation sites for recrystallization increase with increasing rolling strain, which promote the nucleation and growth rates. Additionally, Figure S2 in the Supplementary Material shows EBSD inverse pole figure (IPF) maps with high magnification of the as-hot-rolled sample annealed at temperatures from 275 °C to 350 °C. Interestingly, the orientation of most recrystallized grains was independent of the original orientation of the deformed microstructure.
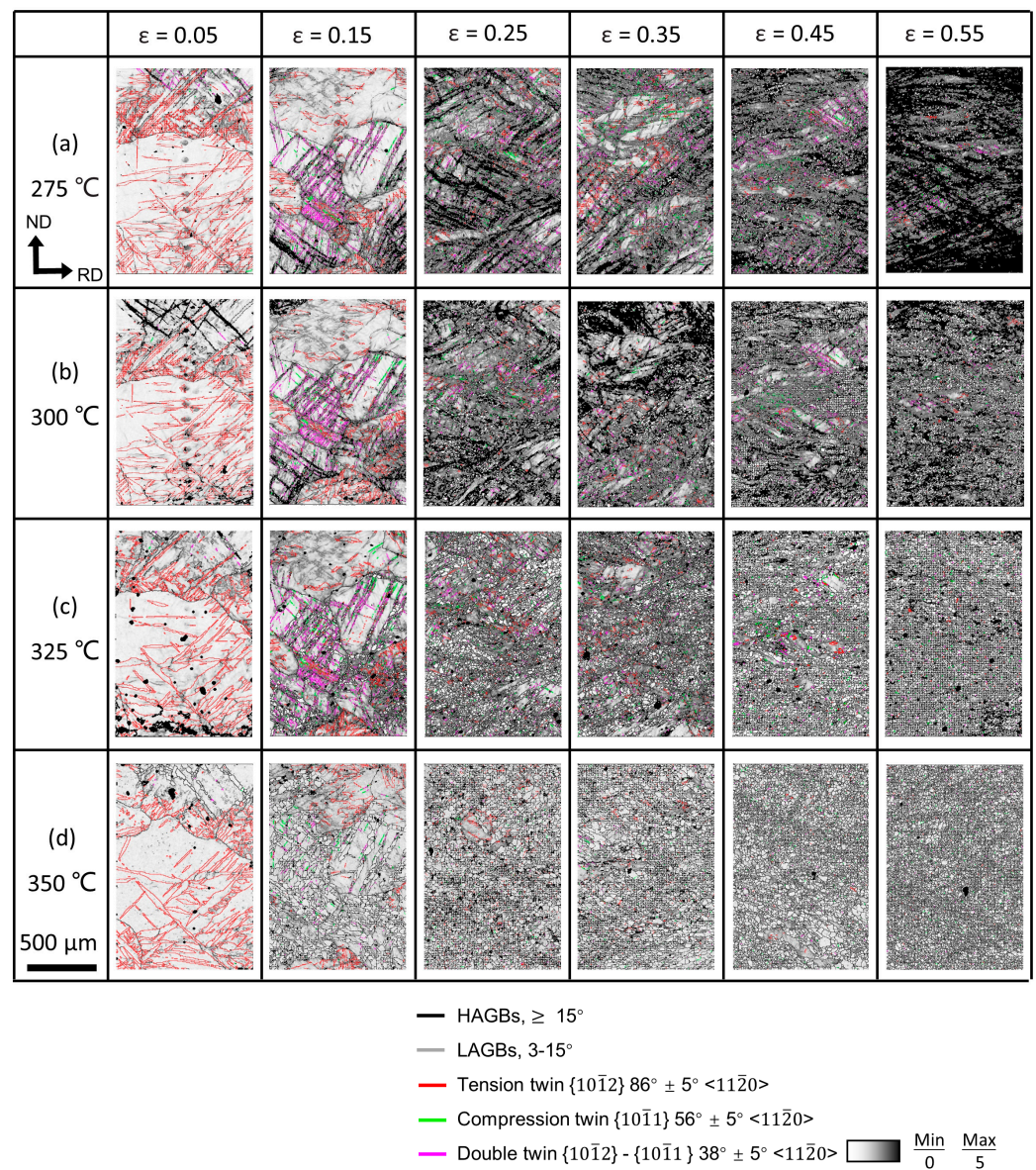
Figure 8. Kernel average misorientation (KAM) maps marked with different twin boundaries of the hot-rolled sample annealed at different temperatures for 1 h: (**a**) 275 °C, (**b**) 300 °C, (**c**) 325 °C, (**d**) 350 °C. HAGBs and LAGBs are marked by black and grey lines, respectively. TTWs, CTWs, and DTWs are marked by red, green, and fuchsia lines, respectively.

Figure 9 shows the {0002} pole figures of the annealed samples with different rolling strains. For the region at $\varepsilon = 0.05$, there was no significant change in all of the textures during annealing from 275 °C to 350 °C, which was consistent with the microstructure as shown in Figure 8. However, for the regions at $\varepsilon = 0.15, 0.25, 0.35, 0.45, 0.55$, the texture intensity decreased with increasing annealing temperature. The higher the rolling strain, the more significant the decrease in texture intensity. For the same annealing temperature, the texture intensity also decreased with increasing rolling strain. The higher the annealing temperature, the more pronounced the weakening of texture. Therefore, the highest volume fraction of recrystallization and the weakest texture were achieved in the sample with a rolling strain of 0.55 after annealing at 350 °C.
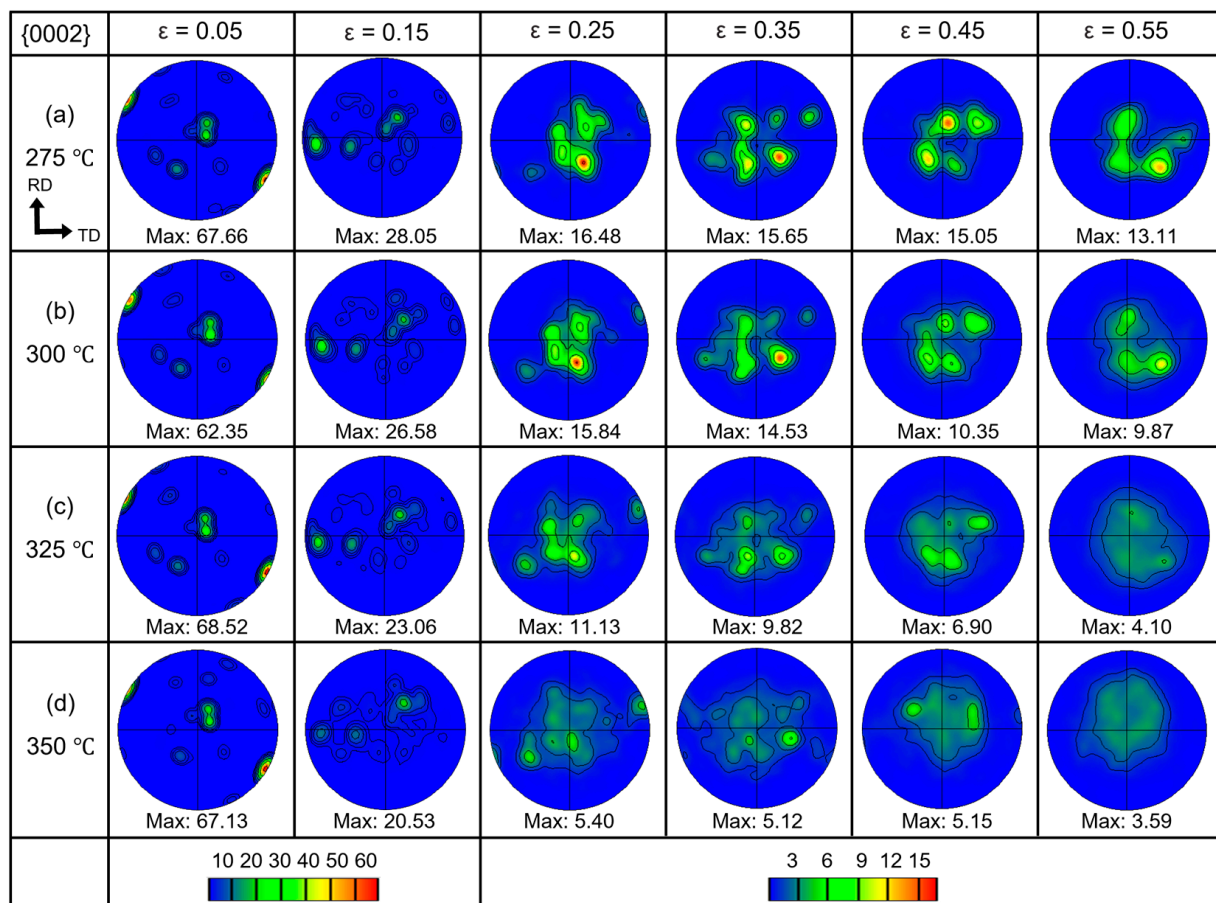
Figure 9. {0002} pole figures of the hot-rolled sample annealed at different temperatures: (**a**) 275 °C, (**b**) 300 °C, (**c**) 325 °C, (**d**) 350 °C.

4. Discussion

4.1. Deformation Mechanisms of Rolled Sample

A gradient-deformed microstructure, that is, from the deformation twins-dominated structures to the shear bands-dominated structures, was observed with increasing the continuous rolling strains along RD, as shown in Figures 3 and 4. Both types of deformed microstructures play an essential role in the subsequent recrystallization process [44,45]. TTWs are readily activated at a very low strains, whereas shear bands are usually observed at high-strain regions in Mg alloys [45,46]. Figure 10 shows the EBSD rate and twin boundaries fraction as a function of rolling strain in the as-hot-rolled sample. The volume fraction of twin boundaries for TTWs, CTWs, and DTWs, and the total twin boundaries in the regions with different rolling strains, are listed in Table 1. With increasing rolling strains, the volume fraction of the total twin boundaries as well as the EBSD indexing rate in the rolled sample decreased, especially for TTWs, while the volume fractions of CTWs and DTWs varied a little. When the rolling strain reached 0.20, the EBSD index rate declined rapidly below 60%, and the volume fraction of the twin boundaries decreased below 10%. Meanwhile, the density of shear bands obviously increased as well, as shown in Figure 4d. The significant change in the EBSD index rate is related to the deformed microstructure, i.e., the microstructure on the left side (Figure 10) with $\varepsilon < 0.20$ is deformation twins-dominated, while the microstructure on the right side with $\varepsilon \geq 0.20$ is shear bands-dominated. Based on the previous studies of the recrystallization behavior in Mg alloys, the preferred nucleation sites during recrystallization differ between the deformation twins-dominated microstructure in the low-strain regions and the shear-bands-dominated microstructure in the high-strain regions [9,28].
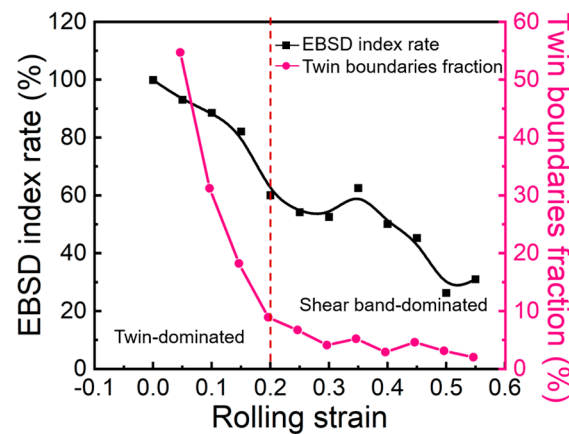
Figure 10. The EBSD index rate and the volume fraction of twin boundaries as a function of rolling strain in the as-hot-rolled sample.

Table 1. The volume fraction of twin boundaries for the as-hot-rolled sample with different rolling strains analyzed from EBSD maps.

Rolling Strain (ε)	The Volume Fraction of Twin Boundaries (%)			
	TTWs	CTWs	DTWs	Total
0.05	53.6	0.2	0.4	54.2
0.10	28.1	0.5	2.1	30.7
0.15	13.3	0.6	3.8	17.7
0.20	5.8	0.6	2.0	8.4
0.25	3.3	0.9	2.0	6.2
0.30	1.0	1.1	1.5	3.6
0.35	2.0	1.4	1.3	4.7
0.40	0.4	0.6	1.4	2.4
0.45	0.5	0.7	2.9	4.1
0.50	1.1	0.5	1.0	2.6
0.55	0.8	0.2	0.5	1.5

4.2. Recrystallization Behavior of Rolled Sample

After annealing, the static recrystallization of the as-hot-rolled sample was triggered, and more recrystallized grains were nucleated with increasing rolling strain, as shown in Figure 8. Accordingly, the relationships among volume fraction and average grain size $(\bar{d})$ of recrystallized grains, rolling strains, and annealing temperatures are shown in Figure 11, and the detailed data are listed in Table 2. For the regions at ε = 0.05, 0.15, 0.25, annealed at 275 °C, and the region at ε = 0.05, annealed at 300 °C, almost no recrystallized grains were found, indicating that these regions mainly recovered. For the regions with an identical rolling strain, the volume fraction and the grain size of recrystallized areas increased with increasing annealing temperature. For the same annealing temperature, the higher the rolling strain, the higher the volume fraction of recrystallization obtained. This is because, with increasing the rolling strain, a higher stored energy accumulated in the deformed matrix, and a faster nucleation and growth rate of recrystallization occurred. When ε = 0.05, the volume fraction of recrystallized grains was only 3.2% and the average grain size was 10.5 ± 5.2 μm, even when annealed at 325 °C, due to the insufficient stored energy [27]. Similarly, when ε = 0.55, the volume fraction of recrystallized grains was also low, i.e., 4.7%, and the average grain size was 7.2 ± 2.2 μm, after annealing at 275 °C, due to the insufficient thermal driving force [43]. Therefore, the recrystallization took place at a higher annealing

temperature in the deformation twins-dominated regions ($\varepsilon < 0.20$) compared with that in the shear bands-dominated regions ($\varepsilon \geq 0.20$). It was easier for the regions with a higher rolling strain to form finer grains and a higher volume fraction of recrystallized grains. Additionally, the growth rate of recrystallized grains in the deformation twins-dominated structures was faster than that in shear bands-dominated structures, as shown in Figure 11b.
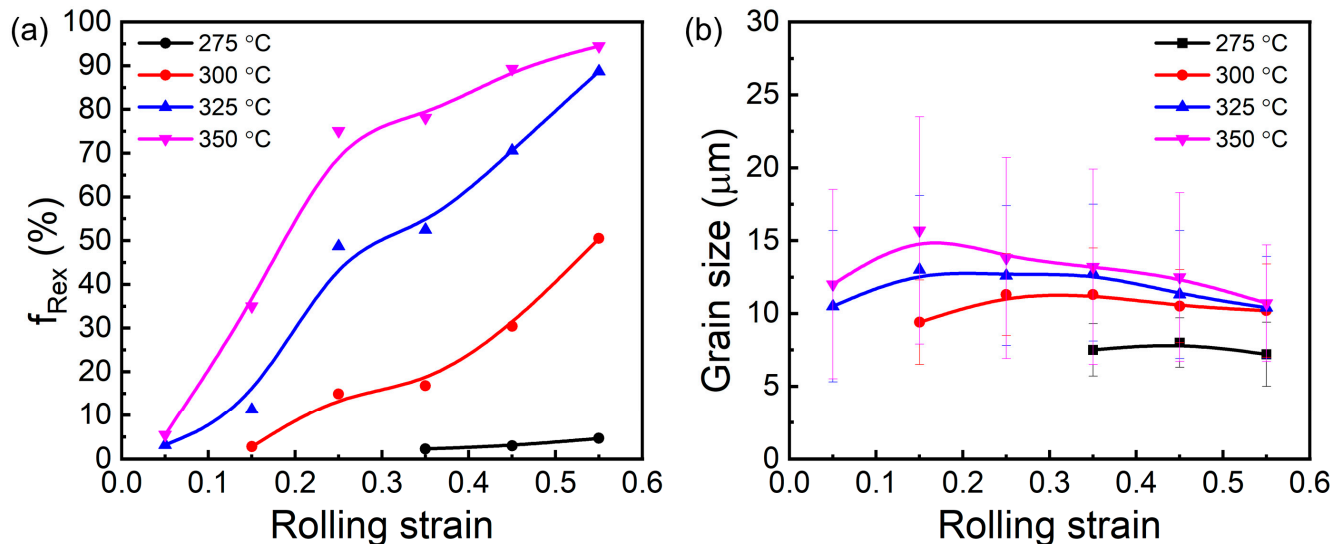

Figure 11. The volume fraction (**a**) and average grain size (**b**) of recrystallized grains as a function of rolling strain for the as-hot-rolled sample annealed at different temperatures.

Table 2. Volume fraction and average grain size of recrystallized grains with different rolling strains and different temperatures (f_{Rex}: the volume fraction of recrystallized grains, $\bar{d}$: the recrystallized grain size).

Rolling Strain		0.05	0.15	0.25	0.35	0.45	0.55
275 °C	f_{Rex} (%)	-	-	-	2.3	3.0	4.7
	$\bar{d}$ (μm)	-	-	-	7.5 ± 1.8	8.0 ± 1.7	7.2 ± 2.2
300 °C	f_{Rex} (%)	-	2.8	14.9	16.8	30.4	50.5
	$\bar{d}$ (μm)	-	9.4 ± 2.9	11.3 ± 2.8	11.3 ± 3.2	10.5 ± 2.5	10.2 ± 3.2
325 °C	f_{Rex} (%)	3.2	11.3	48.7	52.5	70.6	88.7
	$\bar{d}$ (μm)	10.5 ± 5.2	13.0 ± 5.1	12.6 ± 4.8	12.8 ± 4.7	11.3 ± 4.4	10.4 ± 3.5
350 °C	f_{Rex} (%)	5.5	35.0	75.1	78.1	89.3	94.5
	$\bar{d}$ (μm)	12.0 ± 6.5	15.7 ± 7.8	13.8 ± 6.9	13.2 ± 6.7	12.5 ± 5.8	10.7 ± 4.0

The initial deformed microstructure in the as-hot-rolled sample also plays a key role in the recrystallization textures. The {0002} pole figures were obtained from the recrystallized grains with different rolling strains and annealing temperatures, as shown in Figure 12. A weak recrystallization texture formed in all the regions, except the region with $\varepsilon = 0.05$. With increasing rolling strain and annealing temperature, the intensity of textures decreased while the volume fraction of recrystallization increased. For example, a relatively weak texture was achieved after annealing at 325 °C in the region with $\varepsilon = 0.15$, where a few percent to 10% of recrystallized grains was obtained. For the regions with $\varepsilon > 0.20$, the weak recrystallization texture was maintained and its intensity value decreased with increasing annealing time due to the increase in recrystallized grains. It is well known that the recrystallized grains always nucleate at DTWs and CTWs in the deformation twins-dominated regions [9], while the recrystallized grains nucleate inside shear bands in

the shear bands-dominated regions [8]. However, the weak recrystallization texture was formed in almost the entire strain range, indicating that both deformation twins-related and shear bands-related recrystallization led to the weak recrystallization textures.
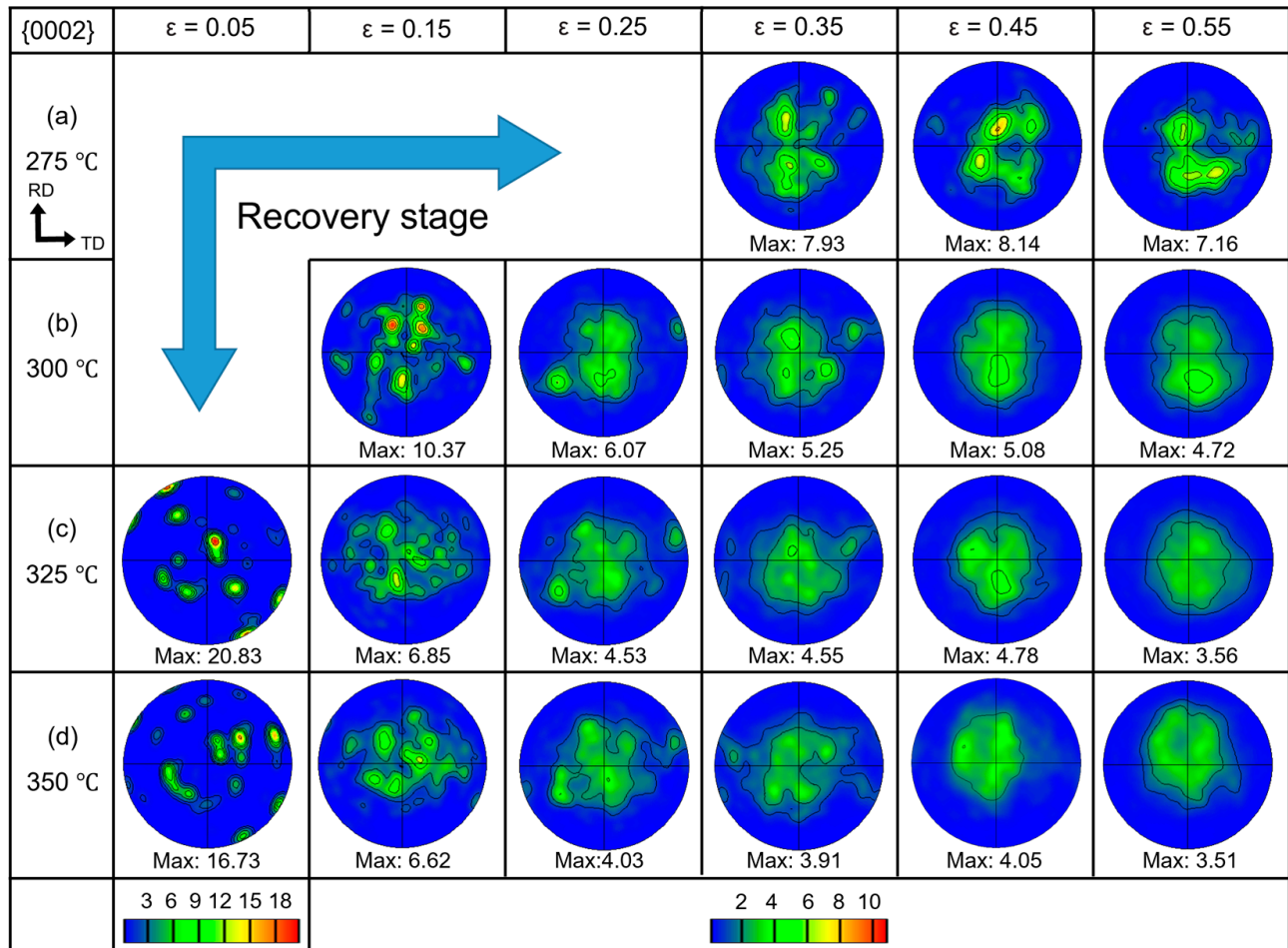

Figure 12. {0002} pole figures consisting only of recrystallized grains at different rolling strains and annealing temperatures: (**a**) 275 °C, (**b**) 300 °C, (**c**) 325 °C, (**d**) 350 °C.

To gain a better understanding of the effect of the orientation distribution of the recrystallized grains in the deformation twins-dominated and shear bands-dominated structures on the final recrystallization textures, the texture of all recrystallized grains is divided into two texture components with orientation deviating ±0–20° and ±20–90° from ND towards RD, respectively. These two texture components are labelled as basal {0002} and non-basal {0002}, respectively. The relationships among the volume fraction of basal {0002} and non-basal {0002} texture components and rolling strains are shown in Figure 13a. The volume fraction of the non-basal {0002} component was much higher than that of the basal {0002} component at different annealing temperatures. Therefore, the volume fractions of the recrystallized grains with orientation deviating ±0–20° from ND towards RD were small, while the majority of the recrystallized grains had orientations that deviated ±20–90° from ND towards RD. Significantly, the average grain sizes of recrystallized grains with basal {0002} and non-basal {0002} orientations were almost the same at the same strain and annealing temperature, as shown in Figure 13b. Meanwhile, all the grain sizes at different strains increased with increasing annealing temperature, although the growth rate of recrystallized grains in the deformation twins-dominated structures ($\varepsilon < 0.20$) was slightly higher than that in the shear bands-dominated structures ($\varepsilon \geq 0.20$) after annealing.
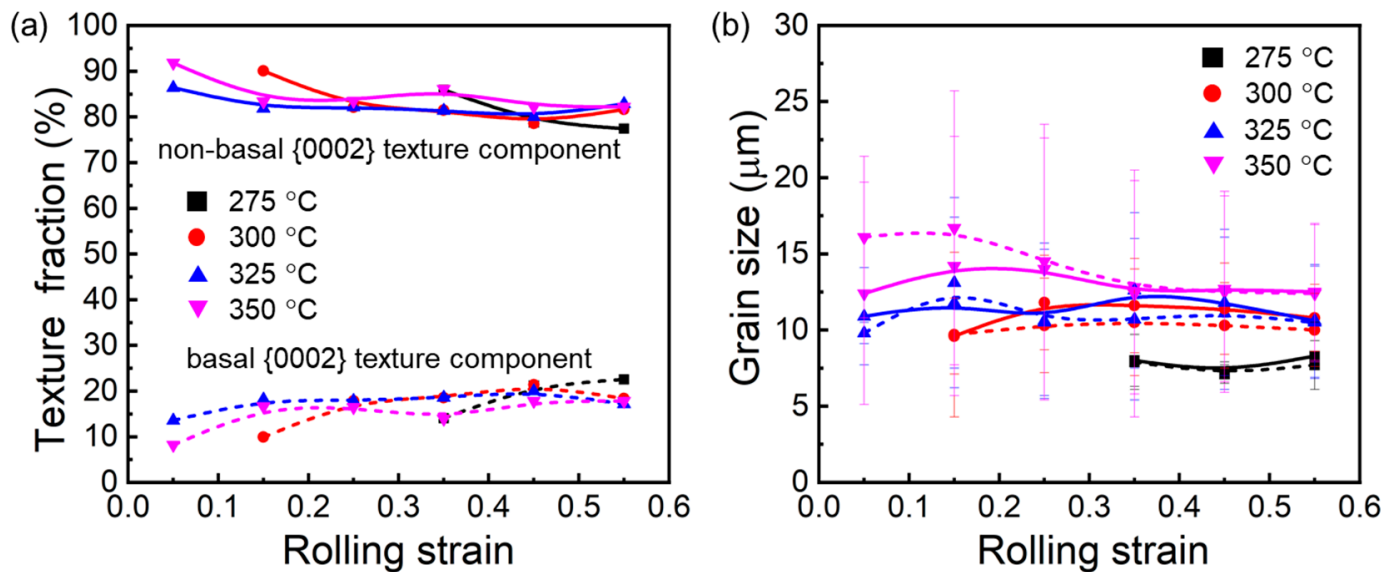
Figure 13. Relationship of basal {0002} (dashed lines) and non-basal {0002} (solid lines) texture components of recrystallized grains related to different rolling strains: (**a**) the volume fraction; (**b**) average grain size at different annealing temperatures.

4.3. The Relationship between Recrystallization Temperature and Rolling Strain

In this work, we analyzed the recrystallization behavior and microhardness of Mg-3Gd alloy at different rolling strains and annealing temperatures. The samples with $\varepsilon = 0.55$ annealed at 325 °C and $\varepsilon = 0.45$ annealed at 350 °C are supposed to have excellent properties after 400 °C hot rolling, and formed fine and equiaxed recrystallized grains with a ~90% volume fraction of recrystallization, as well as weak textures. It is clear that the higher the rolling strain, the lower the recrystallization temperature [47]. This result agrees with the so-called laws of recrystallization formulated by Burke et al. [42]. The effect of rolling strain on the recrystallization temperature can be explained by the stored deformation energy during rolling. When the rolled sample was annealed under the recrystallization temperature, the recrystallization phenomenon was insignificant; when the temperature reached the recrystallization temperature, the recrystallization occurred, and the volume fraction of recrystallization increased with increasing rolling strains and annealing temperatures. The sample with a ~90% volume fraction of recrystallization and extremely weak textures was homogeneous, which is essential for a material with excellent comprehensive properties.

5. Conclusions

(1) With increasing rolling strain, the deformed microstructure gradually varied from deformation twins-dominated structures ($\varepsilon < 0.20$) to shear bands-dominated structures ($\varepsilon \geq 0.20$).

(2) The recrystallization process at different rolling strains can be rapidly tracked and evaluated by the high-throughput characterization of Vickers microhardness before and after annealing.

(3) Compared with the deformation twins-dominated structures, the shear bands-dominated structures generated higher local strain areas to trigger recrystallization nucleation, resulting in a faster nucleation and more homogeneous microstructure.

(4) The high-throughput rolling of Mg-3Gd alloys can be used to study the effect of deformation strain on the deformed microstructure, recrystallization behavior, and subsequent mechanical properties. This strategy can also be extended for high-throughput studies of other metals to accelerate the optimization of processing parameters and microstructural design.

References

1. Sun, J.; Li, B.; Yuan, J.; Li, X.; Xu, B.; Yang, Z.; Han, J.; Jiang, J.; Wu, G.; Ma, A. Developing a high-performance Mg-5.7Gd-1.9Ag wrought alloy via hot rolling and aging. *Mater. Sci. Eng. A* **2021**, *803*, 140707. [CrossRef]
2. Ma, C.-Y.; Xia, N.; Wang, C.; Li, M.-X.; Hua, Z.-M.; Ren, M.-W.; Wang, H.-Y. A novel Mg-5Al-2Zn-2Sn alloy with high strength-ductility synergy fabricated via simple hot rolling and annealing treatment. *J. Alloys Compd.* **2021**, *869*, 159308. [CrossRef]
3. Wang, Y.; Huang, J.C. Texture analysis in hexagonal materials. *Mater. Chem. Phys.* **2003**, *81*, 11–26. [CrossRef]
4. Kaiser, F.; Letzig, D.; Bohlen, J.; Styczynski, A.; Hartig, C.; Kainer, K.U. Anisotropic properties of magnesium sheet AZ31. *Mater. Sci. Forum* **2003**, *419*, 315–320. [CrossRef]
5. Imandoust, A.; Barrett, C.D.; Al-Samman, T.; Inal, K.A.; El Kadiri, H. A review on the effect of rare-earth elements on texture evolution during processing of magnesium alloys. *J. Mater. Sci.* **2017**, *52*, 1–29. [CrossRef]
6. Molodov, K.D.; Al-Samman, T.; Molodov, D.A. Effect of gadolinium on the deformation and recrystallization behavior of magnesium crystals. *Acta Mater.* **2022**, *240*, 118312. [CrossRef]
7. Wu, Z.; Yu, J.; Zhang, Z.; Hu, H.; Zhang, Z. Static recrystallization behavior of Mg-Gd-Y-Zn-Zr alloy during annealing treatment. *JOM* **2022**, *74*, 2566–2576. [CrossRef]
8. Li, L.; Suh, B.-C.; Suh, J.-S.; Kim, C.; Go, Y.; Kim, Y.M. Static recrystallization behavior of the cold-rolled Mg-1Al-1Zn-0.1Ca-0.2Y magnesium alloy sheet. *J. Alloys Compd.* **2023**, *938*, 168508. [CrossRef]
9. Guan, D.; Rainforth, W.M.; Gao, J.; Sharp, J.; Wynne, B.; Ma, L. Individual effect of recrystallisation nucleation sites on texture weakening in a magnesium alloy: Part 1—Double twins. *Acta Mater.* **2017**, *135*, 14–24. [CrossRef]
10. Kim, H.J.; Jin, S.-C.; Jung, J.-G.; Park, S.H. Influence of undissolved second-phase particles on dynamic recrystallization behavior of Mg-7Sn-1Al-1Zn alloy during low- and high-temperature extrusions. *J. Mater. Sci. Technol.* **2021**, *71*, 87–97. [CrossRef]
11. Zeng, Z.R.; Zhu, Y.M.; Xu, S.W.; Bian, M.Z.; Davies, C.H.J.; Birbilis, N.; Nie, J.F. Texture evolution during static recrystallization of cold-rolled magnesium alloys. *Acta Mater.* **2016**, *105*, 479–494. [CrossRef]
12. Lu, S.H.; Wu, D.; Yan, M.; Chen, R.S. Achieving texture randomization and yield anisotropy reduction in rolled Mg-Zn-Y-Zr alloy by multidirectional impact forging. *Mater. Charact.* **2023**, *195*, 112540. [CrossRef]
13. Lee, S.W.; Kim, S.H.; Jo, W.K.; Hong, W.H.; Kim, W.; Moon, B.G.; Park, S.H. Twinning and slip behaviors and microstructural evolutions of extruded Mg-1Gd alloy with rare-earth texture during tensile deformation. *J. Alloys Compd.* **2019**, *791*, 700–710. [CrossRef]
14. Guo, E.; Cao, Y.; Wang, L.; Zhao, S.; Feng, Y.; Fu, Y. Effect of rolling deformation on microstructure and mechanical properties of Mg-Y-Nd-Al alloy. *Mater. Sci. Technol.* **2023**, *39*, 1519–1529. [CrossRef]
15. Nayyeri, G.; Poole, W.J.; Sinclair, C.W.; Zaefferer, S. Measurement of the critical resolved shear stress for basal slip in magnesium alloys using instrumented indentation. *Scr. Mater.* **2018**, *156*, 37–41. [CrossRef]
16. Lee, S.W.; Han, G.; Jun, T.-S.; Park, S.H. Effects of initial texture on deformation behavior during cold rolling and static recrystallization during subsequent annealing of AZ31 alloy. *J. Mater. Sci. Technol.* **2021**, *66*, 139–149. [CrossRef]
17. Zhou, B.; Wang, L.; Wang, J.; Maldar, A.; Zhu, G.; Jia, H.; Jin, P.; Zeng, X.; Li, Y. Dislocation behavior in a polycrystalline Mg-Y alloy using multi-scale characterization and VPSC simulation. *J. Mater. Sci. Technol.* **2022**, *98*, 87–98. [CrossRef]

18. Yao, Y.; Liu, C.; Gao, Y.; Jiang, S. Deformation mechanism of Mg-Gd-Y-Zr alloy during hot ring rolling. *Mater. Charact.* **2021**, *177*, 111154. [CrossRef]

19. Shi, B.Q.; Wang, Y.Z.; Shang, X.L.; Zhao, L.Y.; Li, C.Q.; Chen, D.C.; Nie, B.H.; Chen, R.S.; Ke, W. Microstructure evolution of twinning-induced shear bands and correlation with 'RD-split' texture during hot rolling in a Mg-1.1Zn-0.76Y-0.56Zr alloy. *Mater. Charact.* **2022**, *187*, 111853. [CrossRef]

20. Xiao, B.; Song, J.; Tang, A.; Jiang, B.; Sun, W.; Liu, Q.; Zhao, H.; Pan, F. Effect of pass reduction on distribution of shear bands and mechanical properties of AZ31B alloy sheets prepared by on-line heating rolling. *J. Mater. Process. Technol.* **2020**, *280*, 116611. [CrossRef]

21. Wang, J.; Jin, P.; Li, X.; Wei, F.; Shi, B.; Ding, X.; Zhang, M. Effect of rolling with different amounts of deformation on microstructure and mechanical properties of the Mg-1Al-4Y alloy. *Mater. Charact.* **2020**, *161*, 110149. [CrossRef]

22. Wang, M.; Xin, R.; Wang, B.; Liu, Q. Effect of initial texture on dynamic recrystallization of AZ31 Mg alloy during hot rolling. *Mater. Sci. Eng. A* **2011**, *528*, 2941–2951. [CrossRef]

23. Du, Y.; Zheng, M.; Ge, Y.; Jiang, B.; Shen, M. Microstructure and texture evolution of deformed Mg-Zn alloy during recrystallization. *Mater. Charact.* **2018**, *145*, 501–506. [CrossRef]

24. Li, Y.; Xu, Q.; Ma, A.; Zhang, J.; Shen, Y.; Jiang, J.; Jiang, Y.; Liu, H. Investigations on microstructure and mechanical properties of AZ91 alloy processed by single pass rolling with varied rolling reductions. *Processes* **2023**, *11*, 405. [CrossRef]

25. Dong, J.-B.; Li, K.; Gao, L.-X.; Li, C.-S. Microstructure and properties of Nb, V and N alloyed low magnetic hot rolled stainless steel plate. *Tungsten* **2022**, *166*, 1–10. [CrossRef]

26. Catorceno, L.L.C.; De Abreu, H.F.G.; Padilha, A.F. Effects of cold and warm cross-rolling on microstructure and texture evolution of AZ31B magnesium alloy sheet. *J. Magnes. Alloys* **2018**, *6*, 121–133. [CrossRef]

27. Jin, Z.Z.; Cheng, X.M.; Zha, M.; Rong, J.; Zhang, H.; Wang, J.G.; Wang, C.; Li, Z.G.; Wang, H.Y. Effects of Mg17Al12 second phase particles on twinning-induced recrystallization behavior in Mg-Al-Zn alloys during gradient hot rolling. *J. Mater. Sci. Technol.* **2019**, *35*, 2017–2026. [CrossRef]

28. Guan, D.; Rainforth, W.M.; Gao, J.; Ma, L.; Wynne, B. Individual effect of recrystallisation nucleation sites on texture weakening in a magnesium alloy: Part 2- shear bands. *Acta Mater.* **2018**, *145*, 399–412. [CrossRef]

29. Zhao, J.; Jiang, B.; Xu, J.; He, W.; Huang, G.; Pan, F. The influence of Gd on the recrystallisation, texture and mechanical properties of Mg alloy. *Mater. Sci. Eng. A* **2022**, *839*, 142867. [CrossRef]

30. Ansari, N.; Sarvesha, R.; Lee, S.Y.; Singh, S.S.; Jain, J. Influence of yttrium addition on recrystallization, texture and mechanical properties of binary Mg–Y alloys. *Mater. Sci. Eng. A* **2020**, *793*, 139856. [CrossRef]

31. Zhou, X.; Liu, C.; Gao, Y.; Jiang, S.; Chen, Z. Improved workability and ductility of the Mg-Gd-Y-Zn-Zr alloy via enhanced kinking and dynamic recrystallization. *J. Alloys Compd.* **2018**, *749*, 878–886. [CrossRef]

32. Wang, Y.-Y.; Jia, C.; Xu, M.; Kaseem, M.; Tayebi, M. Microstructural changes caused by the creep test in ZK60 Alloy reinforced by SiCp at intermediate temperature after KOBO extrusion and aging. *Materials* **2023**, *16*, 3885. [CrossRef]

33. Sandlöbes, S.; Zaefferer, S.; Schestakow, I.; Yi, S.; Gonzalez-Martinez, R. On the role of non-basal deformation mechanisms for the ductility of Mg and Mg-Y alloys. *Acta Mater.* **2011**, *59*, 429–439. [CrossRef]

34. Zhang, Z.; Zhang, J.; Xie, J.; Liu, S.; Fu, W.; Wu, R. Developing a Mg alloy with ultrahigh room temperature ductility via grain boundary segregation and activation of non-basal slips. *Int. J. Plast.* **2023**, *162*, 103548. [CrossRef]

35. Mouhib, F.-Z.; Sheng, F.; Mandia, R.; Pei, R.; Korte-Kerzel, S.; Al-Samman, T. Texture selection mechanisms during recrystallization and grain growth of a magnesium-erbium-zinc alloy. *Metals* **2021**, *11*, 171. [CrossRef]

36. He, C.; Jiang, B.; Wang, Q.; Chai, Y.; Zhao, J.; Yuan, M.; Huang, G.; Zhang, D.; Pan, F. Effect of precompression and subsequent annealing on the texture evolution and bendability of Mg-Gd binary alloy. *Mater. Sci. Eng. A* **2021**, *799*, 140290. [CrossRef]

37. Nie, J.F.; Zhu, Y.M.; Liu, J.Z.; Fang, X.Y. Periodic segregation of solute atoms in fully coherent twin boundaries. *Science* **2013**, *340*, 957–960. [CrossRef]

38. Liu, C.; Chen, X.; Tolnai, D.; Hu, Y.; Zhang, W.; Zhang, Y.; Pan, F. Annealing hardening effect aroused by solute segregation in gradient ultrafine-grained Mg-Gd-Zr alloy. *J. Mater. Sci. Technol.* **2023**, *144*, 70–80. [CrossRef]

39. Alfonso, A.; Juul Jensen, D.; Luo, G.N.; Pantleon, W. Recrystallization kinetics of warm-rolled tungsten in the temperature range 1150–1350 °C. *J. Nucl. Mater.* **2014**, *455*, 591–594. [CrossRef]

40. Alfonso, A.; Juul Jensen, D.; Luo, G.N.; Pantleon, W. Thermal stability of a highly-deformed warm-rolled tungsten plate in the temperature range 1100–1250 °C. *Fusion Eng. Des.* **2015**, *98–99*, 1924–1928. [CrossRef]

41. Chen, T.; Sun, M.; Liu, R.; Jiang, W.; Wu, X.; Wang, X.; Liu, C.; Fang, Q. Determination of recrystallization temperature of deformed high-purity Al assessed by internal friction technique. *J. Alloys Compd.* **2022**, *891*, 161984. [CrossRef]

42. Burke, J.E.; Turnbull, D. Recrystallization and grain growth. *Prog. Met. Phys.* **1952**, *3*, 220–292. [CrossRef]

43. Awan, I.Z.; Khan, A.Q. Recovery, recrystallization, and grain-growth. *J. Chem. Soc. Pak.* **2019**, *41*, 1–42.

44. Chen, Y.; Jin, L.; Dong, J.; Zhang, Z.; Wang, F. Twinning effects on the hot deformation behavior of AZ31 Mg alloy. *Mater. Charact.* **2016**, *118*, 363–369. [CrossRef]

45. Guan, D.; Rainforth, W.M.; Ma, L.; Wynne, B.; Gao, J. Twin recrystallization mechanisms and exceptional contribution to texture evolution during annealing in a magnesium alloy. *Acta Mater.* **2017**, *126*, 132–144. [CrossRef]

46. Basu, I.; Al-Samman, T.; Gottstein, G. Shear band-related recrystallization and grain growth in two rolled magnesium-rare earth alloys. *Mater. Sci. Eng. A* **2013**, *579*, 50–56. [CrossRef]

47. Su, C.W.; Lu, L.; Lai, M.O. Recrystallization and grain growth of deformed magnesium alloy. *Philos. Mag.* **2008**, *88*, 181–200. [CrossRef]